Volume 23, No 4 | International Journal of Radiation Research, October 2025

Generation of computed tomography images with different tube voltages by generative adversarial network

H. Takano[1,2*], Y. Kondo[2], Y. Ishizawa[1], S. Onodera[1], M. Saito[2], H. Ota[3]

[1]*Department of Radiological Technology, Tohoku University Hospital, 1-1 Seiryo-machi, Aoba-ku, Sendai, Miyagi, 980-8574, Japan*

[2]*Graduate School of Health Sciences, Niigata University, 746 Asahimachidori 2bancho, Chuo-ku, Niigata City, Niigata, 951-8518, Japan*

[3]*Department of Diagnostic Radiology, Tohoku University Hospital, 1-1 Seiryo-machi, Aoba-ku, Sendai, Miyagi, 980-8574, Japan*

► ***Original article***

***Corresponding author:**
Hirokazu Takano,
E-mail:
hirokazu.takano.a1@tohoku.ac.jp

Received: May 2024
Final revised: December 2024
Accepted: January 2025

Int. J. Radiat. Res., October 2025; 23(4): 873-879

DOI: 10.61186/ijrr.23.4.6

Keywords: *Deep learning, medical image processing, dual-energy scanned projection radiography, pulmonary artery.*

ABSTRACT

Background: Single-energy computed tomography (SECT) requires different energies for disease diagnosis and detection. The patient must be scanned again after the CT scan to obtain other tube-voltage images, causing increased radiation exposure. One method for avoiding rescanning is virtual monochromatic images (VMI) by dual-energy computed tomography (DECT). However, VMI has not proven superior to SECT. Moreover, DECT is not available at all facilities. This study used generative adversarial networks to generate 120 kVp and Sn140 kVp CT images from 80 kVp CT images. ***Material and Methods:*** This study involved 35 patients with pulmonary hypertension who underwent CT scans with DECT. The peak signal-to-noise ratio (PSNR) and structural similarity (SSIM) were calculated to evaluate the difference between the real and pseudo images. Furthermore, the mean CT values of the pulmonary arteries (PA) were compared. ***Results:*** The SSIM was 0.99 ± 9.15×10-5 and 0.99 ± 3.38×10-3 at 120 kVp and Sn140 kVp, respectively. The PSNR was 69.1 ± 1.29 and 66.5 ± 5.40 at 120 kVp and Sn140 kVp, respectively. Additionally, no significant differences were observed in the mean CT values of PA ($p > 0.05$) between the real and pseudo images. ***Conclusion:*** The proposed model accurately generated 120 kVp and Sn140 kVp CT images from 80 kVp CT images.

INTRODUCTION

Routine clinical computed tomography (CT) uses a tube voltage setting of 120 kVp. However, with the development of technology, other tube voltage settings are also being applied clinically [1, 2]. A low tube voltage can enhance the contrast enhancement effect of iodine, which reduces the amount of contrast medium required compared to that for 120 kVp [3-6]. In contrast, a high tube voltage scan reduces metal artifacts and can recover data lost due to photon starvation [7, 8]. Zhang *et al*. reported that high tube voltage, high pitch non-contrast abdominal-pelvic CT significantly reduces patient radiation exposure and scan time while maintaining image quality. This technology avoids artifacts caused by poor breath-holding and accurately identifies urinary stones at a lower dose [9]. However, once the CT scan is complete, the patient must be scanned again to obtain other tube voltage images due to various reasons. In particular, the quality of computed tomography pulmonary angiography (CTPA) is generally suboptimal, resulting in misdiagnosis and uncertainty. CTPA uncertainties range from 0.03 to 10% [10, 11]. Therefore, low-kilovoltage images for improved contrast enhancement are required. However, rescanning requires further radiation exposure and contrast media administration that would become invasive to the patients.

One method for avoiding rescanning is using virtual monochromatic images (VMI) by dual-energy computed tomography (DECT). Lam *et al*. reported that the optimal image signal-to-noise ratio is 65 keV, and 40 keV VMI reconstruction with a high contrast-to-noise ratio is recommended for evaluating patients with head and neck squamous cell carcinoma. They recommend both the standard 65 keV VMI and 40 keV VMIs reconstructions [12]. In the abdominal region, in the single-energy CT (SECT), a hepatic enhancement of at least 50 Hounsfield Unit (HU) is desirable [13]. Noda *et al*. reported that hepatic enhancement (ΔHU > 50 HU) was achieved at 65 keV and 70 keV with 400 mgI/kg and 500 mgI/kg in DECT, respectively [14]. Therefore, once the DECT scan was complete, the VMI could reconstruct any image of the energy required by the user.

In contrast, Sugawara *et al*. reported no significant differences were observed in the visualization of larger arteries, such as the celiac and superior mesenteric arteries. However, VMI obtained with conventional half-iodine had more difficulty detecting smaller arteries and had lower image resolution [15].

[DOI: 10.61186/ijrr.23.4.6]

Additionally, when comparing the low tube voltage of SECT to the VMI of DECT, the optimal scan protocol and extent vary for every CT vendor [16]. Yoshida *et al*. reported that the CT values of the aorta at 70 kVp using two high-power X-ray tubes with an iodine concentration of 180 mgI/kg was lower than that at 40 keV, However, 70 kVp was superior to 40 keV in both objective and subjective image qualities [17]. Therefore, although VMI can acquire many energy images at once, it still faces problems with image quality. Another limitation is that DECT is not available at all facilities.

In addition to VMI, DECT technology can produce iodine map images. Dai *et al.* reported that iodine map images can be optimized tumor response biomarkers in the abdominal region [18]. In the lung region, iodine map images reveal segmental deficiencies in iodine distribution at locations corresponding to vessel occlusion caused by embolism [19-21]. DECT iodine maps have been used in patients with chronic thromboembolic pulmonary hypertension (CTEPH), a type of pulmonary hypertension (PH) [22-24]. Takagi *et al*. reported that the lung perfused blood volume score is a useful and noninvasive estimator of clinical CTEPH severity [25]. DECT requires images in both low and high tube voltages.

Goodfellow *et al.* reported generative adversarial networks (GAN) that can generate a pseudo image equivalent to a real image by competing pseudo images with real ones [26]. Subsequently, a conditional GAN (cGAN), which provides stable learning by applying certain conditions to the input data and enables high-precision image generation, was introduced [27]. Recently, cGAN demonstrated state-of-the-art performance in text-to-image synthesis, super-resolution, and image-to-image conversion [28-31].

In DECT, it has been reported to generate analysis images using DECT from SECT images. Kawahara *et al*. reported that deep convolutional GAN can directly generate VMI that can be reconstructed by DECT from SECT of 120 kVp CT images [32]. Zhao *et al*. reported on the generation of VMI from SECT images using U-net instead of GAN [33]. Funama *et al*. reported on the generation of 55 keV images of VMI from 120 kVp SECT images using pix2pix at 8-bit, 256 × 256 image resolution [34].

In SECT, Zhao *et al*. reported synthesizing high-energy CT (HECT) images from low-energy CT (LECT) images with various neural networks. However, in their study, the images were also 8-bit, 256 × 256 [35]. In GAN, LECT to HECT image generation in SECT images has not been reported under the same conditions as real clinical images at 16-bit and 512 × 512 in the pulmonary vascular region. The significance of this same condition as for clinical images is that the CT value can perform tests of statistical significance between real images and images generated by GAN. If HECT image can be generated from LECT, two different tube voltage images can be obtained, so that DECT technology can be performed at all facilities. The novelty of this study is to generate 16-bit and 512 × 512-pixels HECT images corresponding to clinical CT images from LECT using GAN. In this study, we aimed at generating pseudo 120 kVp and Sn140 kVp images from 80 kVp images in the pulmonary vascular region with GAN without increasing the radiation dose and without using DECT.

MATERIAL AND METHODS

Patients

Chest CT images of 35 patients with PH disease scanned by DECT from April 2013 to December 2019 were used in the experiment. Thirty randomly selected CT data (5867 images) were used as training data, and the remaining five CT scan data (994 images) were used as test data. The training data were used to train the generator and discriminator networks and determine the degree of learning. The trained model was applied to the test data to generate images. Table 1 summarizes the list of target patients. This study was approved in accordance with relevant named guidelines and regulations by the ethical review boards of our institutions (Ethical number: 2023-1-714, Date of registration: December 14, 2023). The institutional review board approved this retrospective study and waived the requirement for obtaining informed consent from the patients.

Table 1. Target patient characteristics.

	Total
Age	69 (39-96)
Sex	6 : 29
Weight [kg]	56.4 (36.0-80.1)
Body Mass Index [kg/m^2]	23.2 (14.5-34.3)

DECT data acquisition and reconstruction

This study used a second-generation dual-source DECT system (SOMATOM Definition Flash; Siemens Healthcare, Germany). All patients in this study scanned with 80 kVp/Sn140 kVp, reference mAs 141/60 mAs, gantry rotation time 0.28 s, pitch 1.0, and section collimation 0.6 mm.

Training and test data for the GAN were obtained from 80 kVp CT images and Sn140 kVp CT images under the dual energy (DE) scan protocol. 120 kVp images were created using the DE composition system from paired datasets of 80 kVp and Sn140 kVp CT images on a CT system. All images were reconstructed at a slice thickness of 2.0 mm with a 2.0 mm interval, using a DE medium-soft convolution kernel (D30f with filtered back projection) in a 28-33 cm display field of view based on the patient's body size.

[DOI: 10.61186/ijrr.23.4.6]

The CT images generated by GAN were defined as pseudo images and the CT images reconstructed with the device were defined as real images. The resolution of both real and pseudo images was 512 × 512 matrix.

Model structure and training

To generate the pseudo 120 kVp and Sn140 kVp CT images, we used pix2pix model reported by Isola *et al.* [36], a modified conditional GAN using MATLAB R2023a (MathWorks, United States). Pix2pix has generator and discriminator architecture. Figure 1 shows the details of the two networks.

The generator network was U-Net, which was an encoder-decoder convolutional neural network with skip connections (figure 2). The discriminator network was a convolutional patch GAN that only penalizes the structure at the scale of image patches (figure 3). For generating the 120 kVp images, a pair of 80 kVp and 120 kVp real images (real-image pairs) and a pair of 80 kVp real images and 120 kVp pseudo image (including pseudo-image pairs) were alternately input to the discriminator. Similarly, for generating the Sn140 kVp imaging, a pair of 80 kVp and Sn140 kVp real images (real-image pairs) and a pair of 80 kVp real images and Sn140 kVp pseudo image (including pseudo-image pairs) were alternately input to the discriminator. An input image was divided into small patch images, which were estimated to be real-image pairs or including pseudo-image pairs. Each patch image extracts features from a convolutional layer. The fully connected layer discriminates each patch image into real-image pairs or including pseudo-image pairs using the softmax function. The result of the discriminator between real -image pairs and including pseudo-image pairs is output by summing the results of all patch images. The training proceeded with the parameters of each network by comparing the output of the discriminator and the correct label. This operation was repeated for all the training datasets. Finally, the generator is trained to generate more realistic pseudo images. Convolution-BatchNormalization-Leaky ReLU style modules were used in the generator and discriminator. The Adam solver training options were set to a learning rate of 0.0002, momentum parameters β1 = 0.5, β2 = 0.999, and 200 epochs.

Quantitative image analysis

After training, this study quantitatively compared pseudo images generated using test data with the real images. The peak signal-to-noise ratio (PSNR) [37] and structural similarity index (SSIM) [38] were calculated to evaluate the difference between the real images and the generated pseudo images. PSNR and SSIM were calculated by equations (1) and (3), respectively.

$$PSNR = 20 \times log_{10}\left(\frac{MAX_f}{\sqrt{MSE}}\right) \quad (1)$$

Where; MAX_f is the maximum pixel value of the image. MSE was determined by equation (2).

$$MSE = \frac{1}{MN}\sum_{i=1}^{M}\sum_{j=1}^{N}(f_{ij} - g_{ij})^2 \quad (2)$$

Where; f and g are real images and pseudo images, respectively. both of size M × N.

Rajkumar *et al.* reported that the standard value of PSNR is 35 to 40 dB, with higher PSNR values indicating better image quality [37].

$$SSIM(CT^{real}, CT^{pseudo}) = \frac{(2 \times \mu_{real} \times \mu_{pseudo} + c_1)(2 \times \sigma_{real,pseudo} + c_2)}{(\mu_{real}^2 + \mu_{pseudo}^2 + c_1)(\sigma_{real}^2 + \sigma_{pseudo}^2 + c_2)} \quad (3)$$

Where; CT_{real} and CT_{pseudo} are the pixel values of the real and pseudo images, respectively. μ_{real} and μ_{pseudo} are the mean values of the real and pseudo images, respectively. σ_{real} and σ_{pseudo} are the standard deviations of the real and pseudo images, respectively. $\sigma_{real,pseudo}$ is the covariance of the real and pseudo images. $c_1 = (0.01 \times L)^2$, $c_2 = (0.03 \times L)^2$; c_1 and c_2 constants that prevent zero denominator and stabilize equation (3). L is the dynamic range of CT value for the real and pseudo images. SSIM is a metric that measures the similarity between a real image and a generated pseudo image. An SSIM value of 1.0 is the highest, indicating high structural similarity. Moreover, SSIM is correlated with human visual perception [38].

CT values of pulmonary arteries

The average CT values of the real and pseudo images at 120 kVp or Sn140 kVp were measured for five cases of test data in the region of interest (ROI). The circular ROI was set at 150 mm^2. For all test data, measurements were taken five times for the main, right, and left pulmonary arteries at different slice locations within the range from the left pulmonary artery upper end to the right ventricular outflow tract. Figure 4, an example of the test data, shows the measurement points.

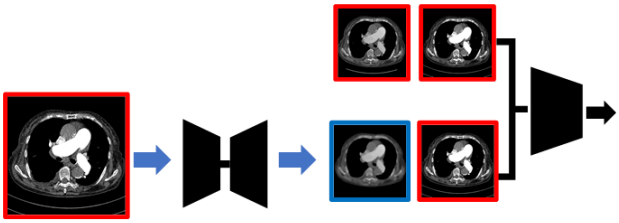

Figure 1. Structure of pix2pix Images surrounded by red lines are real images, and images surrounded by blue lines are pseudo images.

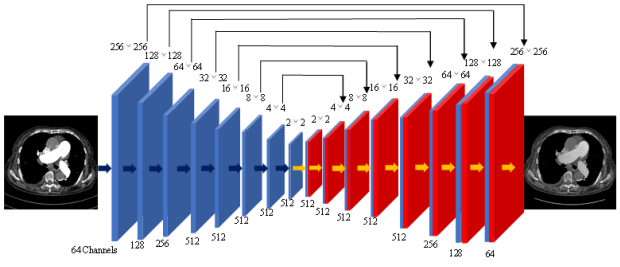

Figure 2. Pix2pix model comprises generator U-Net.

[DOI: 10.61186/ijrr.23.4.6]

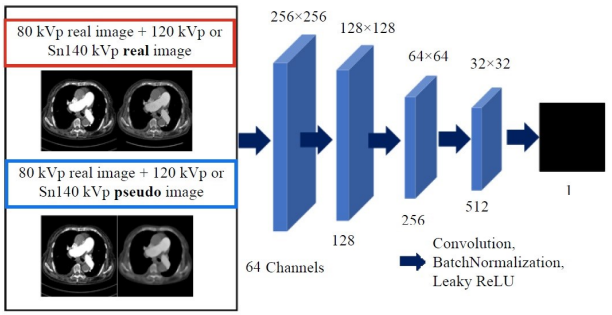

Figure 3. Pix2pix model comprises discriminator Patch GAN.

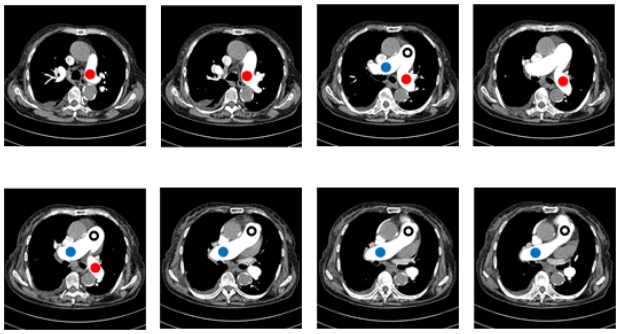

Figure 4. CT value measurement site in one case of test data images of the main, right, and left pulmonary arteries. Red circle: Left pulmonary arteries. Blue circle: Right pulmonary arteries. Black circle: Main pulmonary arteries.

Statistical analysis

A significant difference test was performed using the paired t-test for the average CT value at each position between the real and pseudo images. $p < 0.05$ was considered statistically significant. The JMP Pro 17 (A Business Unit of SAS, United States) was used for statistical significance testing.

RESULT

Quantitative image analysis

Figure 5 shows the real and pseudo images at 120 kVp of a representative case in the test data. Figure 6 shows the real and pseudo images of Sn140 kVp. Figure 7 shows an image of atelectasis with a collapsed left lung. CT images of atelectasis with a collapsed one lung generated good pseudo images.

The SSIM of 120 kVp real and pseudo images in the test data was $0.99 \pm 9.15\times10^{-5}$ and the PSNR was 69.1 ± 1.29. The SSIM and PSNR at Sn140 kVp were $0.99 \pm 3.38\times10^{-3}$ and 66.5 ± 5.40, respectively. The pseudo images at 120 kVp and Sn140 kVp were very similar to the real images, with SSIM close to 1.0 and PSNR > 40 dB.

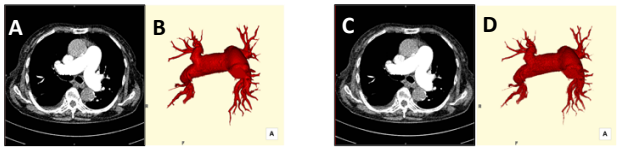

Figure 5. Axial image **(A)** and 3D image of contrast-enhanced pulmonary arteries **(B)** in real image at 120 kVp. Axial image **(C)** and 3D image of contrast-enhanced pulmonary arteries **(D)** in pseudo image at 120 kVp.

Figure 6. Axial image **(A)** and 3D image of contrast-enhanced pulmonary arteries **(B)** in real image at Sn140 kVp. Axial image **(C)** and 3D image of contrast-enhanced pulmonary arteries **(D)** in pseudo image at Sn140 kVp.

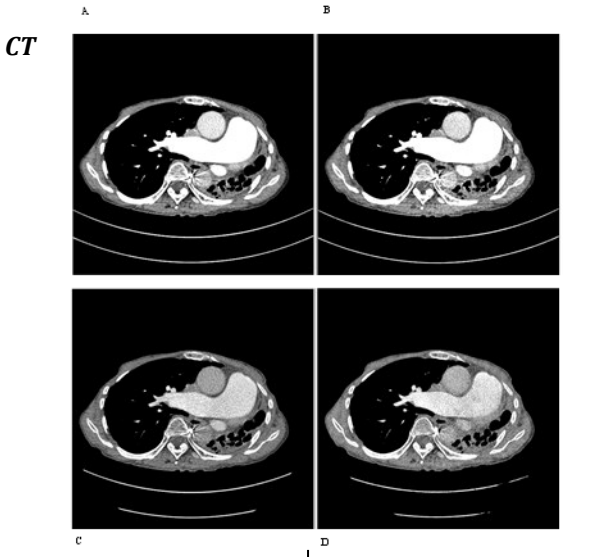

Figure 7. Cases of atelectasis with collapsed left lung and endovascular coil embolization.

values of pulmonary arteries

Table 2 shows the mean CT values of the main, right, and left pulmonary arteries on the real and pseudo images at 120 kVp. The 120 kVp mean CT values did not indicate a statistically significant difference between the real and pseudo images.

Table 3 shows the mean CT values of the Sn140 kVp real and pseudo images. The Sn140 kVp mean CT values did not indicate a statistically significant difference between the real and pseudo images.

Table 2. CT value at 120 kVp.

Target part	Mean CT value (HU) Real image	Mean CT value (HU) Pseudo image	p value
Main PA	373.46±25.19	372.14±24.79	0.71
Rt PA	328.76±40.98	329.34±40.98	0.46
Lt PA	375.42±26.20	377.43±44.10	0.22

Main PA: Main pulmonary artery; Rt PA: Right pulmonary artery; Lt PA: Left pulmonary artery; HU: Hounsfield Unit.

Table 3. CT value at Sn140 kVp.

Target part	Mean CT value (HU) Real image	Mean CT value (HU) Pseudo image	p value
Main PA	240.18±29.33	244.98±27.60	0.21
Rt PA	212.53±30.64	211.47±33.21	0.73
Lt PA	242.67±31.29	241.01±30.21	0.22

Main PA: Main pulmonary artery; Rt PA: Right pulmonary artery; Lt PA: Left pulmonary artery; HU: Hounsfield Unit.

[DOI: 10.61186/ijrr.23.4.6]

DISCUSSION

In this study, pix2pix was used to generate 120 kVp and Sn140 kVp images from 80 kVp images. The pseudo 120 kVp CT and Sn140 kVp images generated from 80 kVp CT images using pix2pix were similar to the real images obtained from DECT scans.

The PSNR at 120 kVp and Sn140 kVp were greater than 40 dB, thereby indicating that the generated pseudo images did not deteriorate and had a sufficiently high image quality. The SSIM value was 0.99. This demonstrates that the pseudo image can be generated to be structurally similar to the real image.

PH of the target lesion in this study refers to elevated pressure resulting from pulmonary arterial remodeling and inflammation or increased downstream pressure [39]. Therefore, this study emphasized the accuracy of CT values in the pulmonary arteries. In this case, CT values were measured in three segments of the pulmonary, main pulmonary, left pulmonary, and right pulmonary arteries. There were no significant differences in the CT values of the pulmonary arteries between the real and pseudo images at 120 kVp and Sn140 kVp.

Li *et al*. proposed a deep learning-based (DL-based) cascaded deep convolutional neural network (CD-ConvNet) structure to simulate pseudo-HECT images from LECT images. They reported that the profiles of pseudo-HECT images from the proposed CD-ConvNet matched well with the profiles of real HECT images [40]. Zhao *et al*. demonstrated a technique to map LECT images to HECT images using a two-stage convolutional neural network (CNN). They reported that the maximum HU difference between the generated HECT images and the real HECT images was 3.47 HU [41]. Both studies, as we did in this study, there was no difference in the similarity between real and pseudo images. However, our study has two specific points compared to the previous studies. First, while the both studies used CNN-based networks, this study used GAN-based networks. The reason is that Charyyev *et al*. have reported that a GAN-based network with additional discriminators enhances realistic synthetic DECT images compared to a CNN-based network [42]. Secondly, the previous studies generated one set of HECT images from LECT images. In contrast, our study generated two sets of HECT images (120 kVp and Sn140 kVp) from a LECT image of 80 kVp.

The test data included cases of atelectasis with a collapsed left lung and endovascular coil embolization. The training data did not include single-lung or metal-coil cases. Pix2pix can generate portraits from sketches, and color palettes from sketches. It is highly sophisticated in generating pseudo data for partial images that do not exist; therefore, pix2pix used in this study generated good pseudo images, even for CT images of atelectasis with a collapsed one lung. To the best of our knowledge, there have been no reports of DL-based models that have generated CT images of atelectasis with lung collapse or of endovascular coil embolization. The advantage of this study is that we were able to generate those CT images using a GAN-based network.

Additionally, we adopted a method to generate images using a high tube voltage from a low tube voltage. Liu CK *et al*. reported that low-to-high kV conversion was superior to high-to-low kV conversion in clinical DECT. The deep learning (DL-based) 140 kVp image generated from the 80 kVp image using DECT had a lower mean squared error between the true and DL-based images [43]. Therefore, an 80 kVp image was used as the input image. However, CT scans at 80 kVp are rarely performed in clinical settings. In the future, the standard tube voltage used in many facilities will be 120 kVp; therefore, 80 kVp and Sn140 kVp pseudo images have to be generated from the 120 kVp tube voltage images.

This study has several limitations. All patients in our study were PH patients only. CT images of normal and other diseased patients have not been evaluated. In addition, we used only pix2pix and did not compare with other GAN-based networks. Moreover, it has not been evaluated whether the generated CT images are useful for diagnosis. These limitations expect to overcome in our future study.

CONCLUSION

Pseudo images with different tube voltages of 120 kVp and Sn140 kVp were generated from 80 kVp CT images using the GAN. The SSIM and PSNR values obtained from the real and pseudo images were high. This study proved the possibility of generating pseudo images with high similarity to real images. The comparison of mean CT values revealed no significant difference between the real and pseudo images. Our study indicated that the GAN could accurately generate 120 kVp and Sn140 kVp CT images from 80 kVp CT images.

Acknowledgment: None.
***Funding*:** This work was supported by a Research Grant of Graduate School of Health Sciences in Niigata University 2022.
***Conflict of interest*:** The authors declare no conflicts of interest.
Ethical consideration: All procedures involving human participants performed in this study were in accordance with the ethical standards of the institutional and/or national research committee and with the ethical standards of the 1975 Helsinki Declaration and its later amendments.
The institutional review board approved this retrospective study and waived the requirement for obtaining informed consent from the patients.

[DOI: 10.61186/ijrr.23.4.6]

***Author contributions*:** H.T., Y.K. and M.S. were involved in the study design. H.T. and S.O. obtained the data. H.T. and H.O. managed data acquisition and storage. Y.I. performed data preprocessing, network training and data analysis. H.T. wrote the initial draft. Y.K., M.S. and Y.I. provided comments and corrections to the draft. H.O. and S.O. provided clinical advice. All authors reviewed, contributed to, and approved the manuscript.

AI usage: We did not use AI in this study.

REFERENCES

1. Mayer C, Meyer M, Fink C, *et al.* (2014) Potential for radiation dose savings in abdominal and chest CT using automatic tube voltage selection in combination with automatic tube current modulation. *Am J Roentgenol*, ***203****(2): 292-299*.
2. May MS, Kramer MR, Eller A, *et al.* (2014) Automated tube voltage adaptation in head and neck computed tomography between 120 and 100 kV: effects on image quality and radiation dose. *Neuroradiology*, ***56****(9): 797-803*.
3. Seyal AR, Arslanoglu A, Abboud SF, Sahin A, Horowitz JM, Yaghmai V (2015) CT of the abdomen with reduced tube voltage in adults: A practical approach. *Radiographics,* ***35****(7): 1922-1939*.
4. Zaehringer C, Euler A, Karwacki GM, *et al.* (2016) Manual adjustment of tube voltage from 120 to 100 kVp during abdominal CT in patients with body weights ≤75 kg: assessment of image quality and radiation dose in a prospective, randomised trial. *Clin Radiol*, ***71****(6): 615.e1-615.e6*.
5. Takahashi Y, Ota H, Omura K, *et al.* (2018) Image quality and radiation dose of low-tube-voltage CT with reduced contrast media for right adrenal vein imaging. *Eur J Radiol*, ***98****: 150-157*.
6. Szucs-Farkas Z, Schibler F, Cullmann J, *et al.* (2011) Diagnostic accuracy of pulmonary CT angiography at low tube voltage: intraindividual comparison of a normal-dose protocol at 120 kVp and a low-dose protocol at 80 kvp using reduced amount of contrast medium in a simulation study. *Am J Roentgenol*, **197**(5): W852-W859.
7. Wu M, Keil A, Constantin D, Star-Lack J, Zhu L, Fahrig R (2014) Metal artifact correction for x-ray computed tomography using kV and selective MV imaging. *Méd Phys*, ***41****(12): 121910*.
8. Hu Y, Pan S, Zhao X, Guo W, He M, Guo Q (2016) Value and clinical application of orthopedic metal artifact reduction algorithm in ct scans after orthopedic metal implantation. *Korean J Radiol*, ***18****(3): 526-535.*
9. Zhang GMY, Shi B, Sun H, *et al.* (2017) High-pitch low-dose abdominopelvic CT with tin-filtration technique for detecting urinary stones. *Abdom Radiol*, ***42****(8): 2127-2134*.
10. Remy-Jardin M, Remy J, Baghaie F, Fribourg M, Artaud D, Duhamel A (2000) Clinical value of thin collimation in the diagnostic workup of pulmonary embolism. *Am J Roentgenol*, ***175****(2): 407-411*.
11. Ruiz Y, Caballero P, Caniego J, *et al.* (2003) Prospective comparison of helical CT with angiography in pulmonary embolism: global and selective vascular territory analysis. Interobserver agreement. *Eur Radiol*, ***13****(4): 823-829*.
12. Lam S, Gupta R, Levental M, Yu E, Curtin HD, Forghani R (2015) Optimal virtual monochromatic images for evaluation of normal tissues and head and neck cancer using dual-energy CT. *Am J Neuroradiol*, ***36****(8): 1518-1524*.
13. Heiken JP, Brink JA, McClennan BL, Sagel SS, Crowe TM, Gaines MV (1995) Dynamic incremental CT: effect of volume and concentration of contrast material and patient weight on hepatic enhancement. *Radiology*, ***195****(2): 353-357*.
14. Noda Y, Goshima S, Nakashima Y, *et al.* (2020) Iodine dose optimization in portal venous phase virtual monochromatic images of the abdomen: Prospective study on rapid kVp switching dual energy CT. *Eur J Radiol*, ***122****: 108746*.
15. Sugawara H, Suzuki S, Katada Y, *et al.* (2019) Comparison of full-iodine conventional CT and half-iodine virtual monochromatic imaging: advantages and disadvantages. *Eur Radiol*, ***29****(3): 1400-1407*.
16. Hamersvelt RW van, Eijsvoogel NG, Mihl C, *et al.* (2018) Contrast agent concentration optimization in CTA using low tube voltage and dual-energy CT in multiple vendors: a phantom study. *Int J Cardiovasc Imaging*, ***34****(8): 1265-1275*.
17. Yoshida M, Nakaura T, Sentaro T, *et al.* (2020) Prospective comparison of 70-kVp single-energy CT versus dual-energy CT: Which is more suitable for CT angiography with low contrast media dosage? *Acad Radiol*, ***27****(5): e116-e122*.
18. Dai X, Schlemmer HP, Schmidt B, *et al.* (2013) Quantitative therapy response assessment by volumetric iodine-uptake measurement: Initial experience in patients with advanced hepatocellular carcinoma treated with sorafenib. *Eur J Radiol,* ***82****(2): 327-334*.
19. Im DJ, Hur J, Han K, *et al.* (2020) Prognostic value of dual-energy CT -based iodine quantification versus conventional CT in acute pulmonary embolism: A propensity-match analysis. *Korean J Radiol*, ***21****(9): 1095-1103.*
20. Foti G, Silva R, Faccioli N, *et al.* (2021) Identification of pulmonary embolism: diagnostic accuracy of venous-phase dual-energy CT in comparison to pulmonary arteries CT angiography. *Eur Radiol*, ***31*** *(4): 1923-1931.*
21. Ko JP, Brandman S, Stember J, Naidich DP (2012) Dual-energy computed tomography concepts, performance, and thoracic applications. *J Thorac Imaging*, ***27****(1): 7-22*.
22. He J, Fang W, Lv B, *et al.* (2012) Diagnosis of chronic thromboembolic pulmonary hypertension: comparison of ventilation/perfusion scanning and multidetector computed tomography pulmonary angiography with pulmonary angiography. *Nucl Med Commun*, ***33****(5): 459-463*.
23. Delcroix M, Torbicki A, Gopalan D, *et al.* (2021) ERS statement on chronic thromboembolic pulmonary hypertension. *Eur Respir J,* ***57*** *(6): 2002828*.
24. Nakazawa T, Watanabe Y, Hori Y, *et al.* (2011) Lung perfused blood volume images with dual-energy computed tomography for chronic thromboembolic pulmonary hypertension: Correlation to scintigraphy with single-photon emission computed tomography. *J Comput Assist Tomogr*, ***35****(5): 590-595.*
25. Takagi H, Ota H, Sugimura K, *et al.* (2016) Dual-energy CT to estimate clinical severity of chronic thromboembolic pulmonary hypertension: Comparison with invasive right heart catheterization. *Eur J Radiol*, ***85****(9): 1574-1580*.
26. Goodfellow IJ, Pouget-Abadie J, Mirza M, *et al.* (2014) Generative Adversarial Networks. *ArXiv Preprint arXiv: 1406.2661.*
27. Mirza M and Osindero S (2014) Conditional Generative Adversarial Nets. *ArXiv Preprint arXiv: 1411.1784.*
28. Yi X, Walia E, Babyn P (2019) Generative adversarial network in medical imaging: A review. *Med Image Anal*, ***58****: 101552*.
29. Yi X and Babyn P (2018) Sharpness-aware low-dose CT denoising using conditional generative adversarial network. *J Digit Imaging*, ***31****(5): 655-669*.
30. Wang Y, Zhou L, Wang L, *et al.* (2018) Locality adaptive multi-modality GANs for high-quality PET image synthesis. *Lect Notes Comput Sc,* ***11070****: 329-337*.
31. Gholamiankhah F, Mostafapour S, *et al.* (2022) Deep learning-based synthetic CT generation from MR images: comparison of generative adversarial and residual neural networks. *Int J Radiat Res,* ***20****(1): 121–130.*
32. Kawahara D, Ozawa S, Kimura T, Nagata Y (2021) Image synthesis of monoenergetic CT image in dual-energy CT using kilovoltage CT with deep convolutional generative adversarial networks. *J Appl Clin Med Phys,* ***22****(4): 184-192*.
33. Zhao W, Lyu T, Chen Y, Xing L (2020) A deep learning approach for virtual monochromatic spectral CT imaging with a standard single energy CT scanner. *ArXiv Preprint arXiv: 2005.09859*.
34. Funama Y, Oda S, Kidoh M, *et al.* (2021) Conditional generative adversarial networks to generate pseudo low monoenergetic CT image from a single-tube voltage CT scanner. *Phys Medica*, ***83****: 46-51.*
35. Zhou H, Liu X, Wang H, *et al.* (2022) The synthesis of high-energy CT images from low-energy CT images using an improved cycle generative adversarial network. *Quantitative Imaging Medicine Surg*, ***12****(1): 28-42*.
36. Isola P, Zhu JY, Zhou T, Efros AA (2017) Image-to-image translation with conditional adversarial networks. *2017 Ieee Conf Comput Vis Pattern Recognit Cvpr. 5967-5976*.
37. Rajkumar S and Malathi G (2016) A Comparative analysis on image quality assessment for real time satellite images. *Indian J Sci Technology,* ***9****(34): 1-11*.
38. Wang Z, Bovik AC, Sheikh HR, Simoncelli EP (2004) Image Quality Assessment: From Error Visibility to Structural Similarity. *Ieee T Image Process*, ***13****(4): 600-612*.

[DOI: 10.61186/ijrr.23.4.6]

39. Sarah B, Ashrith G, Sandeep S. (2021) Evaluation, diagnosis, and classification of pulmonary hypertension. *Methodist DeBakey Cardiovasc J*, **17**(2): 86-91.
40. Li S, Wang Y, Liao Y, *et al.* (2017) Pseudo dual energy CT imaging using deep learning-based framework: Initial study. *ArXiv Preprint arXiv:1711.07118.*
41. Zhao W, Lv T, Gao P, *et al.* (2019) Dual-energy CT imaging using a single-energy CT data is feasible via deep learning. *ArXiv Preprint arXiv:1906.04874*.
42. Charyyev S, Wang T, Lei Y, *et al.* (2021) Learning-based synthetic dual energy CT imaging from single energy CT for stopping power ratio calculation in proton radiation therapy. *Br J Radiol*, **95**: *20210644.*
43. Liu CK, Liu CC, Yang CH, Huang HM (2021) Generation of brain dual -energy CT from single-energy CT using deep learning. *J Digit Imaging*, **34**(1): 149-161.

[DOI: 10.61186/ijrr.23.4.6]